Cerium-doped -Ni(OH)2 hexagon nanosheets: an effective photocatalyst for degradation of the emerging water pollutant naproxen.

To cite this article before publication: Chhabilal Regmi *et al* 2018 *Nanotechnology* in press https://doi.org/10.1088/1361-6528/aace14

Cerium-doped β-$Ni(OH)_2$ hexagon nanosheets: an effective photocatalyst for degradation of the emerging water pollutant naproxen.

C. Regmi[1], E. Maya-Flores[2], S.W. Lee[1], V. Rodríguez-González[2]*

[1]Department of Environmental and Biochemical Engineering, Sun Moon University, Chungnam 31460, Republic of Korea.

[2]División de Materiales Avanzados, IPICYT, Instituto Potosino de Investigación Científica y Tecnológica, Camino a la Presa San José 2055, Lomas 4a. sección 78216, San Luis Potosí, S.L.P., México

E-mail: *vicente.rdz@ipicyt.edu.mx; vicenrg@hotmail.com

Abstract

Nickel hydroxide β–$Ni(OH)_2$ hexagonal nanosheets were synthetized via a hydrothermal exfoliation process. The practical microwave assisted hydrothermal method facilitated obtain layered nickel 3D nanoplates with cerium functionalization in 5h. The as-produced nanostructures were characterized by XRD, XPS, FESEM, FT-IR, PL, UV-vis, and BET techniques. The hydroxilated structures are nano-thick hexagonal plates having sides with 28 nm in length and 5 nm of average thickness. UV and PL irradiation was used to study the photoactive properties in the degradation of a pharmaceutical emerging pollutant, naproxen. UV-vis spectroscopy and high-performance liquid chromatography (HPLC) monitoring indicated that the $Ni(OH)_2$-Ce nanostructures are an effective photocatalyst for naproxen degradation including 40 % of mineralization of this highly recalcitrant drug. The photocatalyst showed stability for two consecutive cycles, preserving its photoactive and structural characteristics. Ce^{3+} doped nanoplates and surface functionalized Ce^{4+} act as charge separators and scavenging agents for the enhanced photodegradation of naproxen.

Keywords: Nickel hydroxide β–$Ni(OH)_2$; hexagonal nanosheets; hydrothermal exfoliation; naproxen degradation; Cerium-doped $Ni(OH)_2$; HRTEM

Introduction

Transition-metal-oxide-based structures have been used mainly for electrochemical, metal-O_2 battery applications and solar and fuel cell applications due to *d-d* electron transitions that give the electrical, electrochemical and structural properties for these applications [1-4].

In the case of nickel layered materials, they have been reported as *p*-type semiconductors [4-7] which present various types of disorders, including hydration, stacking fault disorders, mechanical stresses and the incorporation of ionic impurities due to detrimental hydration. Two known polymorphs, denoted as α-$Ni(OH)_2$ and β-$Ni(OH)_2$, can describe the majority of nickel hydroxides and related materials with different morphologies [4-5] from one dimensional to three dimensional. As layered double hydroxides (LDHs), the surface charge of nickel hydroxides can be tailored by substituting interlayer cations and anions.[8]

Several synthesis methods and different nickel precursors have defined the crystalline arrangements that have widespread the application spectra.[4, 8] Recently, the exfoliation of ultrathin brucite-like nickel layers was reported as an excellent process to improve the charge−discharge properties of this material in strong alkaline electrolytes[9] and also as boosted oxygen evolution catalysts [10-11] due to the superior electronic conductivity of single layer nanosheets.

Cerium-doped- $Ni(OH)_2$ have narrowly reported mostly for pseudocapacitor applications, [12] Ce^{3+} doping has shown to improve the conductivity which enhances the electrochemical performance and cycling stability. Ce:NiO/rGO sol-gel nanostructures show enhanced electrochemical performance, which is believed to be due to the distortion of crystal lattice caused by doping of Ce into NiO. [13] The formation of Ce^{3+} and Ce^{4+} species in $Ni(OH)_2$ shows good room temperature ferromagnetism.[14] $Ni(OH)_2/CeO_2$ composites are very active for dry reforming of CH_4 with CO_2. The enhanced catalytic performance is attributed to the unique structure of 10 nm Ni nanoparticles stabilized within mesoporous $CeNi_xO_y$.[15] The Ce-$Ni(OH)_2$ materials show average specific surface area of 70 m^2/g, and cerium improves the electronic transference and the increased oxygen mobility. Ce-doped NiO nanomaterial is a useful platform for electrochemical, catalytic and biosensing applications such as riboflavin (RF) detection and bacterial inhibition for *B. subtilis* and *S. aureus*. [16]

As for the electro-catalytic properties of nickel oxides, nickel-hydroxide-based materials have been applied recently to electrocatalytic processes[17-18] and photocatalysis, especially as a TiO_2 heterojunction in thin films.[19-20] Hydrogen production for water splitting reactions[20-22] and dye wastewater treatments [23] are some of the reported photocatalytic applications.

The photocatalytic degradation of emerging pharmaceutical pollutants has become one of the most imperative green technologies[24-25] due to the fact that pharmaceutical compounds are used indiscriminately to control human diseases like pain from various conditions such as headaches, muscle aches, tendonitis, dental pain, etc.[26] Among these compounds, naproxen is one of the most common human-non-steroidal-anti-inflammatory drugs (NSAIDs) that is excreted and flushed into lavatories, having endocrine-active effects associated with harmful potential effects on wildlife and human health due to its persistence in the wastewater environment.[25, 26]

In the present paper, the photoactivity of nickel nanoplates for the degradation of naproxen in aqueous medium under UV irradiation is studied. The photocativity and nanostruture of nickel hydroxide was tailored using a cerium ion in order to change the structural characteristics of the hydroxides and *d-d* electronic transfer. Well-defined, hexagonal plates were characterized by HRTEM, HAADF and FESEM microscopies; XPS and TPR-H_2 helped define the oxidation state and XRD gave the structural crystalline phase. Kinetic photodegradation investigations revealed the occurrence of pseudo-first-order reactions for the most active exfoliated nanoplate for 2 cycles.

Experimental Section

Materials

Naproxen, 2-(6-methoxy-2naphthyl) propanoic acid, was purchased from Sigma-Aldrich (98%), and acetonitrile (HPLC grade, Fermont), acetic acid (99%, Sigma-Aldrich), nickel(II) sulfate hexahydrate (Sigma-Aldrich), sodium hydroxide (Sigma-Aldrich), cerium(III) nitrate hexahydrate, (Alfa-Aesar, 99.99%), iron(III) nitrate nona-hydrate, (Acors Organic 99+%) and ultrapure water supplied by a MilliQ water system were used as eluents.

Hydrothermal synthesis of nickel oxide structures

Nickel hydroxide nanostructures were synthesized by a hydrothermal method using nickel sulfate as precursor (7.038 g, $NiSO_4.6H_2O$) solution were dissolved slowly in 7 M NaOH (70 mL) alkaline solution with vigorous stirring (700 rpm) for 1 h, obtaining a green solution. Simultaneously, an appropriate amount of cerium nitrate was dissolved in 30 mL of water to obtain 3, 5, and 10 wt. % of cerium. The colorless cerium solution was added dropwise to the alkaline solution under constant magnetic stirring and 5 min of sonication in order to assure disaggregation. Then, the green solution

was transferred to a 100 mL Teflon-lined microwave reactor (Eyela MWO-1000 Wave Magic) and heated by microwave irradiation at 120°C for 4 h, 600 rpm, and a maximum variable microwave irradiation power of 200 W. The reactor was cooled down gradually to room temperature. The as-obtained pale green precipitate was washed with distilled water and ethanol several times, and then it was recovered using a rotary evaporator at 80°C. The powder was dried at 80 °C overnight in an oven and annealed at 200°C using a heating ramp of 2°C min^{-1} in order to eliminate the organic part and solvents from the precursors.

For comparison purposes, a 30 mL iron nitrate solution to obtain 5 wt. % of iron was used, carrying out similar steps to those featured in the cerium doping procedure. The synthesized samples were labeled as NiH-CeX, where X represents either Ce or Fe wt. %.

Characterization of nickel oxide nanostructures

The structural characterization of the obtained oxides was carried out using a Rigaku D/Max 2200 HR X-ray Diffractometer equipped with CuKα radiation of λ= 1.5406 Å operated at 40 kV and 40 mA over the interval ranging from 10 to 70°. Morphology and semiquantitative composition analyses were performed by energy dispersive X-ray spectroscopy (EDS) in a FE-SEM (FE-SEM, Helios Double Beam 600 high resolution, operated at 5 kV with an opening of 86 pA). Microstructure, morphology and lattice structures were observed using a high resolution transmission electron microscope (HR-TEM, FEI Tecnai F30 equipped with a tungsten field emission gun operated at 300 keV). Energy gap values were estimated by means of a UV–vis spectrophotometer UV-Vis-DRS JASCO V570 equipped with a diffuse reflectance system. PL measurement were performed on a spectrophotometer (FLS980, Edinburg Instruments, UK) fitted with a photomultiplier tube (PMT) detector (Hamamatsu). The excitation source was a standard 450 watt Xenon lamp. The surface composition was investigated by X-ray photoelectron spectroscopy (XPS, Multilab 2000 system equipped with an X-ray AlKα source operated at 15 kV and 1 mA, 400W). FTIR spectra, in the range between 4000 and 500 cm^{-1}, were recorded in transmittance mode on a Vertex-70 spectrophotometer. On the other hand, N_2 adsorption–desorption measurements were carried out using a Nova 3200 gas-sorption system, which has the flexibility to implement multiple methods of analysis at the same time such as multipoint BET and pore size distribution by the BJH method of desorption isotherms.

Naproxen degradation

The photocatalytic evaluation was performed in a home-made laboratory photoreactor containing 250 mL of a naproxen aqueous solution (20 ppm) and 0.06 g of the nickel nanostructure. The solution was maintained at room temperature and under strong magnetic stirring (1150 rpm) in the dark for 1h in order to ensure the adsorption-desorption equilibrium of naproxen molecules on the photocatalyst surface. Afterwards, the solution was irradiated with UV light using a Hg-lamp emitting at 254 nm, which was plunged into the center of the naproxen solution. 3 mL samples were taken every 15 minutes and filtered through a 0.45 μm nylon filter to displace the catalyst.

Analytical Methods

Naproxen concentration was monitored using a UV-vis spectrophotometer (UV-Vis-NIR of Agilent Technologies Cary 5000), and a HPLC spectrometer (Shimadzu) equipped with a diode array UV/Vis detector (254 nm) and a C18 L Phenomenex column (5 μm, 300 x 3.9 mm, i.d.), which was used for the separation, with an injection volume of 10 μL and acetonitrile/1 % acetic acid (50/50, v/v) as mobile phase, flowing at 1.2 mL min^{-1} and employing an isocratic mode with UV-vis detector set at 230 nm. Naproxen mineralization was determined with a TOC analyzer model TOC-LCSN Shimadzu.

Results and Discussion

The crystalline phase was determined by X-ray diffraction, and the XRD patterns are shown in Figure 1. The main crystalline phase is β–$Ni(OH)_2$ with a hexagonal layered structure (JCPDS 014-0117); the β–phase consists of well-stacked-brucite-like layers in the *c* direction, where normally the 001 peak is associated with the distance between layers. [7, 27] Intensity and width differences of XRD peaks can be observed. As the doping with Ce^{4+} started, the intensity decreased and the peak became slowly broader maybe due to the cerium incorporation which caused some strain between layers. Actually, a peak at 2 theta equal to 28.7 corresponding to the main peak (111) of a cubic-fluorite-type structure of CeO_2 (JCPDS 00-004-0593) was identified. At a load of 10 wt. % of cerium, the peak corresponding to the (220) plan of CeO_2 is also observed at 2 theta equal to 47.77. No diffraction peaks from other nickel phases or impurities are distinguished in the XRD patterns. The crystallite size was calculated by the Scherrer equation from the 001 reflection and the values for all the samples are listed in Table 1. As it can be observed in Figure 1, only the layered NiH-Ce3 material presents an asymmetrical 001 peak shifted slightly to lower angles due to interlayered

stuck cations. The other samples show no uniform strain, which broadens the peak in the *c* direction. It is also observed that the (100) and (101) peaks were not broadened because they have a perpendicular direction to the *c*-axis, and the *ab*-plane is unaffected by stacking faults.[4, 7] In the hexagonal structure from the lattice parameter, *c* is twice the interlayer separation. This parameter is listed in Table 1 and gives some insight about the space for some possible guest molecules. Similar undoped β–$Ni(OH)_2$ with high crystallinity, synthetized by the hydrothermal method at 180°C for 8h, [7] and other analogous intersheet distance were reported for well-crystallized β-$Ni(OH)_2$ with structural disorder. [4, 27]

The structural disorder effects can have very important practical consequences according to the guest atom that replaces some nickel sites. [4, 7, 28] Soft calcination evacuated the interchange water, organic compounds and solvents used during the synthesis of the layered structures. The identification of peaks corresponding to CeO_2 must consider the growth of some CeO_2 over the nickel-brucite-like plates and/or freely after wide-range exfoliation of layers. If some trivalent cations of Ce^{3+} or Ce^{4+} replaced some Ni^{2+}, the resulting composite must be hydroxide-rich [4, 29] with proton-deficient zones, needing some interlayer anions to compensate the charge.

The morphology was studied by FE-SEM microscopy in order to characterize the layered structures and effects of the cerium-doped materials, Figure 2. A well-defined-facet-symmetric-hexagonal-prism shape was the most observed geometry in un-doped NiH samples with thin hexagonal prism plates with an average edge length of 40 nm and a thickness of 8 nm for individual exfoliated plates, Figure 2a). Most of the plates are stacked in columns of maximum 80 nm. In addition, some plates grew as truncated triangles; these plates are relatively rare, Figures 2a)-b). Uniform hexagonal flake-like was obtained by NaOH precipitation under a microwave hydrothermal after calcining at 450 °C for 3 h. Researchers report that method MW hydrothermal method enhanced crystallinity and strong alkaline medium produces β–$Ni(OH)_2$ as preferred product. [28] Synthesis of $Ni(OH)_2$ hexagonal nanocolumns by a facile wet chemical method has similar morphology in 4-8h. [18]

By doping with cerium, the average size was more homogenous and the plates seemed further exfoliated with edge lengths of 28 and 35 nm for NiH-Ce5 and NiH-Fe5, respectively. The size is similar for all the cerium loads; likewise, the morphology was not changed, however, in the NiH-Ce10 sample, some short CeO_2 nanorods can be distinguished, Figures 2c)-d); [30] as a detrimental effect of cerium excess, some $Ni(OH)_2$ layers are no complete exfoliated, see size distribution data in supplementary information Fig S1 to S3.

The XRD results support this fact, where cerium allows the exfoliation of nickel layers in a hydrothermal environment, and the doping decreases the size of the exfoliated nanoplates. The

XRD peaks ascribed to CeO_2 cubic phase start to be distinguished from 3 wt. % of cerium load; at 10 wt. % of cerium, two peaks of the cerium phase can be clearly observed.

The TEM observation in Figure 3a confirms the β-$Ni(OH)_2$ thin hexagonal plates obtained by hydrothermal precipitation with the (001) plane detected as a planar face growth of the plates, [31] Figure 3a-b). Thin hexagonal plates are observed for NiH-Ce5 with the lattice fringe of 0.27 nm that correspond to the (001) plane of β-$Ni(OH)_2$. The plates featured in the present work are much smaller than those reported as ultrathin-1-nm-thick-hexagonal nickel-hydroxide microsheets exfoliated for 24h using a traditional hydrothermal method with dodecyl sulfate ions as exfoliation agents. [9] Moreover, by using a hydrothermal process for 2 days at 150°C in the presence of urea and triethanolamine, single-layered double hydroxides with average thickness of 0.8 nm and side size of around 1 μm were obtained. [10]. Growth of β-$Ni(OH)_2$ structures normally results in nanoslice shape, which is due to growth along the [001] direction of a hexagonal single crystal. [18] Therefore, thickness and uniformity of the plates depends of the method of synthesis.

In Figure 3b), the stacked brucite-like layers and also the hexagonal contour can be observed. The HAADF image shows the transparence of layers, confirming exfoliation and the in-set EDS shows the composition. Figure 3d). β-$Ni(OH)_2$ with 10 % of cerium load presents both morphologies: exfoliated hexagonal plates and short nanorod-like CeO_2.[30]

The nitrogen physical adsorption-desorption characterization of the β-$Ni(OH)_2$ nanostructures revealed type IV isotherms with slight H1 hysteresis loops according to the BDDT classification, Figure 4a). The isotherms show a classical behavior for layered materials, like loose-packed $Ni(OH)_2$ nanoflakes, [17] featuring a sharp hysteresis loop from 0.55 to 0.95, which indicates the presence of microporosity and mesoporosity [31] and confirms the layered brucite-like arrangement. The bare NiH shows only 13 m^2g^{-1} of surface area, which is mainly due to the space between stacked layers [17]. As expected for the observed layered nature, the typical β-$Ni(OH)_2$ samples had a low surface area[31], which is increased almost four times with the cerium incorporation, 53 m^2g^{-1}, which is mainly due to the exfoliation of layers and the decrease in the hexagonal plate size, Table 1. The flat hysteresis loop for high pressure ~0.75-1 P/P_0 is attributed to the transitional pores, which diameters depends from the type of cerium cations and morphology incorporate. As it was pointed in SEM characterization, a detrimental effect of cerium excess, the nickel layers are no complete exfoliated decreasing the surface area to 47.8 m^2g^{-1} with 10% wt. of Ce loading. In this way, the mesoporosity decreases and so affects the surface specific area. The formation of micro-spherical β-$Ni(OH)_2$ superstructures composed of nanosheets was reported in the range of 100 m^2g^{-1}. [17, 31]

The UV-vis spectra of these green colored nickel oxides correspond to the split between the *d-d* orbitals and the bands from the oxidation state coordination in the nickel layer. [4, 20-32] Normally, β–Ni$(OH)_2$ has a coordination number of 6 that means the formation of octahedral configuration with oxygen atoms known as a metal hydroxide with edge sharing octahedral layers. [4, 9, 32] Undoped NiH presents only four weak absorption bands and the energy band-gap is calculated from the split at 350 nm by linearization of the UV-vis optical spectra of the energy axis equal to zero for direct allowed transitions, inset in figure 4b).

Cerium causes perturbation in the nickel coordination, where such perturbations in the Ni(II) coordination sphere appear as a new band centered at 300 nm and slightly red-shifted with hypochromic effect as the cerium load was increased, which is due to the $3A_{2g}(F) \rightarrow 3T_{1g}(P)$ transition of Ni^{2+} in an octahedral system.[4, 32] The absorption band at around 666 nm corresponds to the $3A_{2g}(F) \rightarrow 3T_{1g}(F)$ transition. [20, 27-32] Furthermore, the estimated band-gap energy was slightly decreased with the cerium load increase. [23, 32, 33-34]

The separation efficiency of the photogenerated electrons and holes are investigated by PL spectra. A broad PL band centered nearby 470 nm is observed for all the samples. The PL intensity for Ce doped samples shows a strong decrease as compared to the undoped material. The strong emission of NiH is expected due to the intrinsic luminescence as a result of recombination of electrons and holes. Moreover, the lower PL peak intensity for the optimum 5% of Ce dopant concentration in the NiH lattice is the indication of improved charge separation that supports the improved photocatalytic activity which matches well with our photocatalytic degradation result. When the loading of Ce is increased to 10 % again the PL bands increases. The increase in the PL bands is a detrimental effect of formation of cerium bars due to the excess of cerium loading that segregates to the surface and contribute to the decrease of the number of Ni$(OH)_2$ layers, which affects negatively the surface specific area of the materials. Similarly, the PL band centered at 470 nm is associated with the oxygen vacancy created as a result of doping of Ce, figure 4 c [36-37].

The β-Ni$(OH)_2$ infrared spectrum is shown in Figure 4d). This spectrum shows the typical features of β-Ni$(OH)_2$. A very sharp band located at around 3632 cm^{-1} is due to OH groups in the nickel-brucite-like structure. Broad and small bands at 3435 cm^{-1} correspond to the O-H vibration of a hydrogen-bonded water molecule which exists mainly in the interlamellar space of β-Ni$(OH)_2$ which are more intense in NiH-Ce5. [23, 29, 31] The weak band at 2362 cm^{-1} is a vibration due to nitrate bond anions that remain in the interlayer from the cerium precursor. The band at around 1630 cm^{-1} is assigned to the bending mode of the interlayer water molecule, which is only visible in the cerium nickel samples. The weak transmission bands located at around the 1500-900 cm^{-1}

region are due to intercalated carbonate and nitrate groups; those around 1490 cm^{-1} are attributed to carbonate ions. [31] The bands at around 620, 592 and 482 cm^{-1} are due to the δOH and νNi–OH bending and stretching vibrations [27, 29]; markedly, the bare NiH hydroxide bands are more intense, and cerium incorporation to the brucite–like layers only weakened the transmittance intensity. The characterization of cerium incorporation is not possible with this vibrational technique. The FTIR results provided evidence of the presence of some intercalated nitrate and carbonate ions [29, 31, 35], which results from the precursors and may compensate the rich protonated surface charge of brucite-like layers. Therefore, the nickel hydroxide composition can be represented by the β-$Ni(OH)_2$ phase as it was ascribed beforehand by the XRD analysis.

Photocatalytic naproxen degradation.

The influence of Ce and Fe cations on the photocatalytic activity of the nanoplates is shown in Figure 5. Photocatalytic degradation effectiveness of NPX by NiH and doped NiH-Ce and NiH-Fe is higher than photolysis: more than 84 % for NiH materials and only 76 % in the case of photolysis for 180 min of irradiation. After the incorporation of Ce cations, the samples showed enhanced photocatalytic activity, notably the NiH-Ce5 nanomaterial, achieving 95% of NPX degradation, Table 2. The enhanced photocatalytic performance of NiH-Ce5 is clearly distinguish since the 30 min.

The photocatalytic activity of the catalysts certainly depends on modified surface properties, absorption properties, and crystallinity. In the case of NiH-Ce, the enhanced photocatalytic activity can be discussed according to the parameters mentioned above: firstly, the absorption wavelength range of the doped NiH-Ce catalyst was blue-shifted, which can facilitate the absorption of more photons and the UV photocatalytic activity is improved. Secondly, the beneficial effect of Ce^{3+} should be explained by considering the efficient separation of photoexcited electrons and holes, the increased specific surface area and hydroxilated surface of the layered structure. It is interesting to note that the photocatalytic activities decreased with the increase in Ce^{3+} load up to 5 wt. % and also with the cerium load decrease. The optimum Ce^{3+} concentration was 5 wt. %

Cerium cations are also essential to match the thickness and size of exfoliated layers. Then the better the charge separation, the better the mass diffusion. Only the load of 3wt. % retracts the interlayer distance according to the strain effect observed in the XRD patterns. The increase in the PL bands is a detrimental effect of formation of cerium bars, which affects negatively the surface specific area of the materials. The cerium bars also alter the photoactivity, restraining the e^--h^+ charge separation.

To get more insights about the morphology of the hexagonal layered plate effect, similar hexagonal cerium plates doped with 5 wt. % of nickel were prepared (an inverse system CeO-Ni5), showing that the photoactivity was not enhanced and revealing the importance of the synergism of the cerium ion doping the nickel hexagonal plates. In addition, the nickel layered structures were doped with 5 wt. % of iron, but no enhanced activity was achieved. Morphology seems to exert a negligible effect on the NPX degradation; only cerium ions loaded at 5 wt. % on the layered nickel morphology achieved the NPX degradation. The cerium, nickel and iron ions achieved hexagonal plates, exfoliation and optimized the edge size for improved surface area and favored the photocatalytic process, but did not reach the total degradation.

The presence of Ce, Ni and O elements in the β-$Ni(OH)_2$ plates is confirmed by the X-ray photoelectron spectroscopy (XPS). The chemical state of the Ni was verified by using a high-resolution XPS spectrum of the Ni 2p region as shown in Figure 6. There are two major peaks with binding energies at 866.16 and 860.36 eV, which correspond to Ni $2p_{1/2}$ and Ni $2p_{3/2}$ of $Ni(OH)_2$ with a separation of 17.6 eV, respectively; a further small peak at 855.52 eV was assigned to metallic Ni; in addition, two satellite peaks were fitted by using Shirley background. [4, 37-38] It seems that cerium incorporation to the layers does not change the distribution of nickel and oxygen species, and all the samples show analogous composition states: (i) the identified nickel species are Ni-$(OH)_2$, Ni-O, and metallic Ni, (ii) the oxygen species contained in the layered nickel materials are OH, O-Ni, C=O and C-O; these results agree well with literature data and FTIR results; [27, 29, 31, 36] in Figure 6, the fitting of the Ni 2p and O 1s spectra for the bare NiH and the most active samples are shown.

The determination of the cerium species incorporated into the doped hydroxides by fitting resulted in Ce^{4+} and Ce^{3+}; Figure 7a)-b) shows the assignation of *u* and *v* sub-bands that represent cerium with 4+ and 3+ valences, respectively. [30, 39] The fitting of the Ce3d doublet clearly shows how the load of cerium increased the valence 3+, which confirms that the equilibrium favors the charge separation of e^--h^+, which was achieved with 5% of Ce, Figure 7b). According to the XRD results in the NiH-Ce3 sample, most of the incorporated cerium ions are loaded between the layers as Ce^{3+} and with the increase to 5 wt. % of Ce, some Ce^{4+} are grown on the surface of the brucite-like-nickel layers; more than 5 wt. % causes cerium segregation and formation of small CeO_2 cuboids during the synthesis with detrimental photoactivity effects. [30] Interlayered Ce^{3+} may retard the formation of the CeO_2 phase, allowing the exfoliation of thin hexagonal plates until Ce^{3+} is segregated to form CeO_2 short nanorods as identified by XRD, XPS and TEM.

Loading cerium in the interlayered vacancies with different cerium states favors the electronic transference during the photocatalytic process $Ce^{4+} + e^- \rightarrow Ce^{3+}$ and boosts transfer and constrains the charge recombination.

Hence, the doping with 5 wt. % of cerium cations achieves the degradation of NPX in 180 min and increases its mineralization; the stability and detrimental hydration of layered platelets help the second NPX degradation achieving 75 % of degradation, more than photolysis, Figure 8. The adsorption effect was evaluated because it was reported that NPX can be reversibly intercalated into a layered double hydroxide, [40-41] but in the case of NiH-Ce5, negligible adsorption occurred. Phenol degradation was reported using Ce incorporated into the structure of ZnAl LDH, achieving a mineralization of 95% in 4h, where 20% is due to adsorption. [42] Cerium cations play a photocatalytic enhancement role due to the e^--h^+ reception, avoiding recombination. In our case, the total degradation of a more recalcitrant NPX molecule notable start around 90 min and was achieved in 3 h without apparent irreversible adsorption, reaching 40% of mineralization. NiO obtained by calcination at 800 °C of NiH and NiH-Ce5 does not show more photodegradtion than photolysis, which remarks the importance of double layered hydroxide-rich structures for the photoactivity performance. UV-vis, PL spectra and XRD characterization before and after naproxen degradation confirms a good stability of the samples. However, SEM shows the same hexagonal 3D plates morphology after naproxen degradation, with some damages in side, may due to cerium species lixiviation. Fig S4 to S6. Weak decrease in XRD peaks intensity could be attributed to the loss sample after recovering and dried after the second photocatalytic performance.

In order to ascertain the degradation sub-products and the possible selectivity, the reaction was analyzed by HPLC chromatography for the most active catalyst and photolysis. Figure 9 shows the HPLC chromatogram for the NiH and NiH-Ce5 samples at different irradiation times.

Four peaks are identified; at the start of the reaction, an intense HPLC peak at 7.4 min that corresponds to the naproxen drug is observed. At 15 min of reaction, 4 additional peaks are detected and must correspond to intermediaries or sub-products, which were identified as PD1, PD2, PD3 and PD4, where PD stands for “photoproduct” and the number refers to the order of retention time. In the three cases, the peak assigned to naproxen is abruptly decreased until almost disappearing in the first 75 min. NiH-Ce5 chromatograms only show 3 sub-products at 6.3 (PD2), at 8.5 (PD3) and at 10.3 min (PD4). For NiH and photolysis, an extra product is observed at 5.5 min (PD1), which is the product with the lowest concentration, confirming the role of cerium cations in layered nickel

hydroxide structures during the photoreaction. In Table 3, a quantification of photoproducts is listed and expressed as selectivity obtained from the integrated area of each compound peak.
Naproxen presents direct photolysis due to the fact that these absorption bands are in the UV region. In the literature, NPX degradation reports 4 major products: [43-44] (i) 1-(6-methoxy-naphthalen-2-yl) ethanol; (ii) 2-(6-methoxy naphthalen-2-yl) propanoic acid; (iii) 1-(6-methoxy naphthalen-2-yl) ethanone or methyl 2-(6-methoxy-naphthalen-2-yl) propanoate; and (iv) 2-ethyl-6-methoxy naphthalene. This identification of the naproxen photoproducts was carried out by HPLC from photoproducts irradiated under 3.25 $mWcm^{-2}$ Hg lamps for 3 days. [45]

Mainly, decarboxylation and demethylation are the proposed pathways. [45-47] Demethylation leads to product (i) according to our UV-vis spectra as a function of time, and normally, demethylation is responsible for the slight hyposochromic shifts of the main absorption band from 232 to 228 nm, assuming that this photo-transformation may correspond to the PD2 material. The demethylation process continues until achieving the complete NPX demethylation. In addition, the methyl groups are removed one by one, as it can be confirmed by the gradual wavelength shifts of the maximum-peaks toward the blue region. [45, 47-48] In the case of decarboxylation, it leads to the formation of 2-ethyl-6-methoxynaphthalene (PD4). [44-45, 48] In general, the two pathways occurring simultaneously are due to the photolysis and photocatalytic effects.
It seems that for the NiH-Ce5 nanocomposite, the process is more direct and less organic intermediaries are formed during the photocatalytic exposure. To know the percentage of mineralization of NiH and NiH-Ce3, NiH-Ce5, and NiH-Ce10 and photolysis, an analysis of total organic carbon (TOC) was determined with aliquots taken after 180 min. The calculated initial TOC value is 15.14 mgL^{-1}. Thus, according to the TOC values for NiH-Ce5, mineralization is higher in comparison with other hydroxides and 12% superior than photolysis (Table 2).

The identification of products will help improve the limited understanding of their potential unintended environmental impact and the ecological effects on receiving environments, which remain largely unknown. A full study by UPLC-MS results necessary in order to achieve this issue and further improve the design of nickel hydroxide to be focused on the complete mineralization of NSAID drugs.

The incorporation of foreign anions into β-$Ni(OH)_2$ materials has been reported to be far less common because adjacent layers are close-packed. Furthermore, some modification of the stacked hydroxide and beneficial exfoliated hexagonal platelet for photocatalytic drug degradation and

mineralization was confirmed by XPS and XRD characterizations. In addition, the possible coexistence of α/β-interstratification could not be detected because the degree of the α-phase could be out XRD detection.

Conclusions

Hexagonal $Ni(OH)_2$ ultrathin plates were synthesized by a facile hydrothermal homogeneous exfoliation method without using any surfactant or complex precursor in 5 h. Well-defined facets with a truncated symmetric hexagonal shape were obtained.

The incorporation of cerium species into the nickel layered hydroxide: i) reduces the size of nickel hexagonal plates to 28 nm, attaining their exfoliation in contrast with bare $Ni(OH)_2$, ii) cerium cations (Ce^{3+} and Ce^{4+}) enhance the electronic transfer from layers to cations for the degradation of the NSAID drug, iii) these cations, intercalated water and anions produce a positively charged framework that allows the oxygen cleavage, and iv) the load of 5% of cerium achieves the total degradation within 3 h, achieving 40 % of mineralization, v) the catalysts can be reused for one more cycle, achieving 75 % of degradation, showing good aqueous stability.

Novel two-dimensional thin layers with significantly improved surface activity, compared with their bulk, layered counterparts will be useful for advanced treatment technologies, preferably have to be immobilized in low-dense support or use in photo-electrodes, via AOPs using these stable and cheaper materials commonly used in electrochemical or magnetic processes.

Acknowledgements

We gratefully acknowledge G. Labrada-Delgado, B. Rivera-Escoto and H. Silva Pereyra from LINAN-IPICYT for the FESEM, XRD and HRTEM characterizations. The authors thank R. Camposeco for helping with the fitting of XPS spectra and G. Muñoz Moreno for assistance in photocatalytic degradation during summer stage. E. Maya-Flores thanks CONACyT-IPICyT for the postdoctoral fellowship. V.R.G thanks KOFTS for the Brain Pool Program No. 152S-2-31424. This research was partially supported by the National Research of Korea (NRF) funded by Ministry of Education, Science and Technology (Grant number: 2010-00339).

References

[1] C. Yuan, H. B. Wu, Y. Xie, X. W. Lou, *Angew. Chem. Int. Ed. Engl*. **2014**, *53*, 1488-1504.

[2] J. Meyer, S. Hamwi, M. Kroger, W. Kowalsky, T. Riedl, A. Kahn, *Adv. Mater*. **2012**, *24*, 5408 - 5427.

[3] A. Blackman, S. E. Bottle, S. S. Schmid, M. Mocerino, U. Wille, *Chemistry, 3rd Edition*, Wiley, 2015, p. 546.

[4] D. S. Hall, D. J. Lockwood, C. Bock, B. R. MacDougall, *Proc. R. Soc. A* **2014**, *471*, 20140792.

[5] X. Ma, Y. Li, Z. Wen, F. Gao, C. Liang, R. Che, *ACS Appl. Mater. Interfaces* **2015**, *7*, 974-979.

[6] M. D. Irwin, D. B. Buchholz, A. W. Hains, R. P. H. Chang, T. J. Marks, *Proc. National Academy of Sciences. USA* **2008**, *105*, 2783 - 2787.

[7] A. J. Khan, D. O'Hare, *J. Mater. Chem.* **2002**, *12*, 3191-3198.

[8] F. Dionigi, T. Reier, Z. Pawolek, M. Gliech, P. Strasser, *ChemSusChem* **2016**, *9*, 962 - 972.

[9] S. Ida, D. Shiga, M. Koinuma, Y. Matsumoto, *J. Am. Chem. Soc.* **2008**, *130*, 14038 - 14039.

[10] F. Song, X. Hu, *Nature Communications* **2014**, *5*, 4477.

[11] H. Liang, F. Meng, M. Caban-Acevedo, L. Li, A. Forticaux, L. Xiu, Z. Wang, S. Jin, *Nano Lett*. **2015**, *15*, 1421 - 1427.

[12] Anjali P, Vani R, Sonia T S, Nair A S, Ramakrishna S, Ranjusha R, Subramanian K R V., Sivakumar N, Mohan C G, Nair S and Balakrishnan A, *Sci. Adv. Mater*. **2014**, 6 94–101

[13] Gawali S R, Dubal D P, Deonikar V G, Patil S S, Patil S D, Gomez-Romero P, Patil D R and Pant J, *ChemistrySelect* **2016** 1 3471–8

[14] J. C. Bear , P. D. McNaughter, P. Southern, P. O'Brien, C. W. Dunnill, *Crystals* **2015**, 5, 312-326

[15] Dou J, Bao Z and Yu F, *ChemCatChem*, **2018** 10 250–8

[16]. P. Muthukumaran, C. V. Raju C, C. S, G. R, D. S, P. R, J. W, Rajendran S and Alwarappan S *New J. Chem*. **2016**, 40, 2741 – 2748

[17] G. X. Tong, F. T. Liu, W. H. Wu, J. P. Shen, X. Hu, Y. Liang, *Cryst. Eng. Comm*. **2012**, *14*, 5963 - 5973.

[18] X. Zhang, A. Gu, G. Wang, B. Fang, Q. Yan, J. Zhu, T. Sun, J. Ma, H. H. Hng, *Cryst. Eng. Comm*. **2011**, *13*, 188 - 192.

[19] J. Yu, W. Wang, B. Cheng, *J. Chem. Asian* **2010**, *5*, 2499 - 2506.

[20] J. Yu, Y. Hai, B. Cheng, *J Phys Chem*. C **2011**, 4953 – 495

[21] J. Ran, J. Zhang, J. Y, M. Jaroniecc, S. Z. Qiao, *Chem. Soc. Rev*. 2014, 43, 7787 - 7812

[22] C. G. Morales-Guio, M. T. Mayer, A. Yella, S. D. Tilley, M. Grätzel, Xile Hu, *J. Am. Chem. Soc*. **2015**, *137, 9927−9936.*

[23] F. Motahari, M. R. Mozdianfard, F. Soofivand, M. Salavati-Niasari, *RSC. Adv*. **2014**, *4*, 27654 -27660.

[24] H. Zhang, P. Zhang, Y. Ji, J. Tian, Z. Du, *Chem. Eng. J.* **2015**, *262*, 1108 - 1115.

[25] M. P. Sammartino, M. Castrucci, D. Ruiu, G. Visco, L. Campanella. *Chem. Central J.* **2013**, *7*,181

[26] S. Yan and W. Song, *Environ. Sci.: Processes Impacts*, **2014**, 16, 697

[27] V. Rodriguez- Gonzalez, E. Marceau, M. Che, C. Pepe, *J. Solid State Chem*. **2007**, *180*, 3469-3478.

[28] L. Xu, Y. S. Ding, C. H. Chen, L. Zhao, C. Rimkus, R. Joesten. S. L. Suib, *Chem. Mater*. **2008**, *20*, 308 - 316.

[29] D. S. Hall, D. J. Lockwood, S. Poirier, C. Bock, B. R. MacDougall, *J. Phys. Chem. A* **2012**, 116, 6771−6784

[30] S. L. Clavijo-Chaparro, A. Hernández-Gordillo, R. Camposeco-Solis, V. Rodríguez-González, *J. Mol. Cat. A: Chem*. **2016**, *423*, 143-150.

[31] C. Coudun, F. Grillon, Jean-Francois Hochepied, *Colloids Surf. A: Physicochem. Eng. Aspects* **2006**, 280, 23 – 31.

[32] Y. Qi, H. Qi, J. Li, C. Lu, *J. Crys. Growth* 2008 *310* 4221– 4225

[33] Z. Zhu, N. Wei, H. Liu, Z. He, *Adv. Powder. Technol*. **2011**, *22*, 422 - 426.

[34] C. W. Kim, Y. S. Son, A. U. Pawar, M. J. Kang, J. Y. Zheng, V. Sharma, P. Mohanty, Y. S. Kang, *J. Mater. Chem. A* **2014**, *2*, 19867 - 19872.

[44] A. K. Mondal, D. Sua, S. Chen, J. Zhang, A. Ung, G. Wang, *Chem. Phys. Lett.* **2014**, 610–611, 115–120

[36] T. N. Ramesh, A. Taj, *Int. J. Sci. Res*. 2013, 1, 487-494

[37] S. Kumar, A. K. Ojha, *RSC Adv*. **2016**, *6*, 8651–60

[38] J. F. Moulder, W. F. Stickle, P. E. Sobol, K. D. Bomben, *Handbook of X-ray Photoelectron Spectroscopy*, Perking-Elmer Corp., Physical Electronics Division, Eden Prairie, MN, **1992**.

[39] M. C. Biesinger, B. P. Payne, L.W.M. Lau, A Gerson, R St. C. Smart, *Surf. Interface Anal.* **2009**, 41, 324–332

[40] A. Khan, L. Lei, A. J. Norquist, D. O'Hare, *Chem. Commun*. **2001**, *22*, 2342 - 2343.

[41] E. Aranya, R. K. Szabó, L. Apáti, T. Alapi, I. Ilisz, P. Mazellier, A. Dombi, K. Gajda-Schrantz, *J. Hazard. Mater*. **2013**, *262* 151 – 157.

[42] M. Suarez-Quezada, G. Romero-Ortirz, V. Suarez, G. Morales-Mendoza, L.L. Lartuno-Rojas, E. Navarro-Ceron, F. Tzompantzi, S. Robles, R. Gomez, A. Mantilla, *Catal. Today* **2016**, *271*, 213 - 229.

[43] J. L. Packer, J. J. Werner, D. E. Latch, K. McNeill, W. A. Arnold, *Aquat. Sci.* **2003** 65 342 – 351.

[44] N. Jalloulia, K. Elghniji, O. Hentatia, A. R. Ribeirod, A.M.T. Silvad, M. Ksibi, *J. Hazard. Mater.* **2016** *304* 329 – 336.

[45] Y. H. Hsu, Y. B. Liou, J. A. Lee, C. Y. Chen, A. B. Wu, *Biomed. Chromatogr.* **2006**, *20*, 787-793.

[46] K. T. Rao, L. V. Rao, *Am. J. Anal. Chem.* **2013**, *4*, 286 – 292.

[47] F. Mendez-Arriaga, J. Gimenez, S. Esplugas, *J. Adv. Technol*. **2008**, *11*, 435 - 444.

[48] D. Kanakaraju, C. A. Motti, B. D. Glass, M. Oelgemöller, *Chemosphere* **2015** *139* 579 – 588.

Figures Caption

Figure 1. XRD patterns of a) different nickel layered hydroxides doped with Ce and Fe, b) zoomed range of the d_{001} plane which is directly related to stacked-brucite-like layers.

Figure 2. FESEM images of the hexagonal-well-shaped prism of β-$Ni(OH)_2$ at different cerium loads: (a) undoped NiH , (b) NiH-Ce5, (c) NiH-Fe5, and (d) NiH-Ce10 all at 200 000 magnifications.

Figure 3. Transmission electron microscopy focused on high resolution of the nanoplates in HRTEM and HAADF modes: (a) NiH-Ce5, (b) NiH-Ce5 magnifications, (c) HAADF plus punctual EDS and (d) NiH-Ce10.

Figure 4. (a) N_2 physisorption isotherms, (b) UV-Vis-DRS reflectance spectra, (c) PL spectra and (d) FTIR spectra of nickel layered hydroxides.

Figure 5. Photocatalytic degradation of NPX as a function of time by the different layered materials.

Figure 6. O1s and Ni 2p XPS spectra of undoped Ni-hydroxide materials and with a cerium load of 5 wt. %

Figure 7. Ce 3d XPS spectra of Ni-hydroxide materials and with a cerium load of 3 and 5 wt. %

Figure 8. NPX degradation profiles for the two reaction cycles with NiH-Ce using the same catalyst powder.

Figure 9. HPLC chromatograms of a naproxen solution during photocatalytic reaction at 0, 15, 30, 45, 60, 75 and 90 min: a) photolysis, b) NiH and c) NiH-5Ce

Fig. 1.

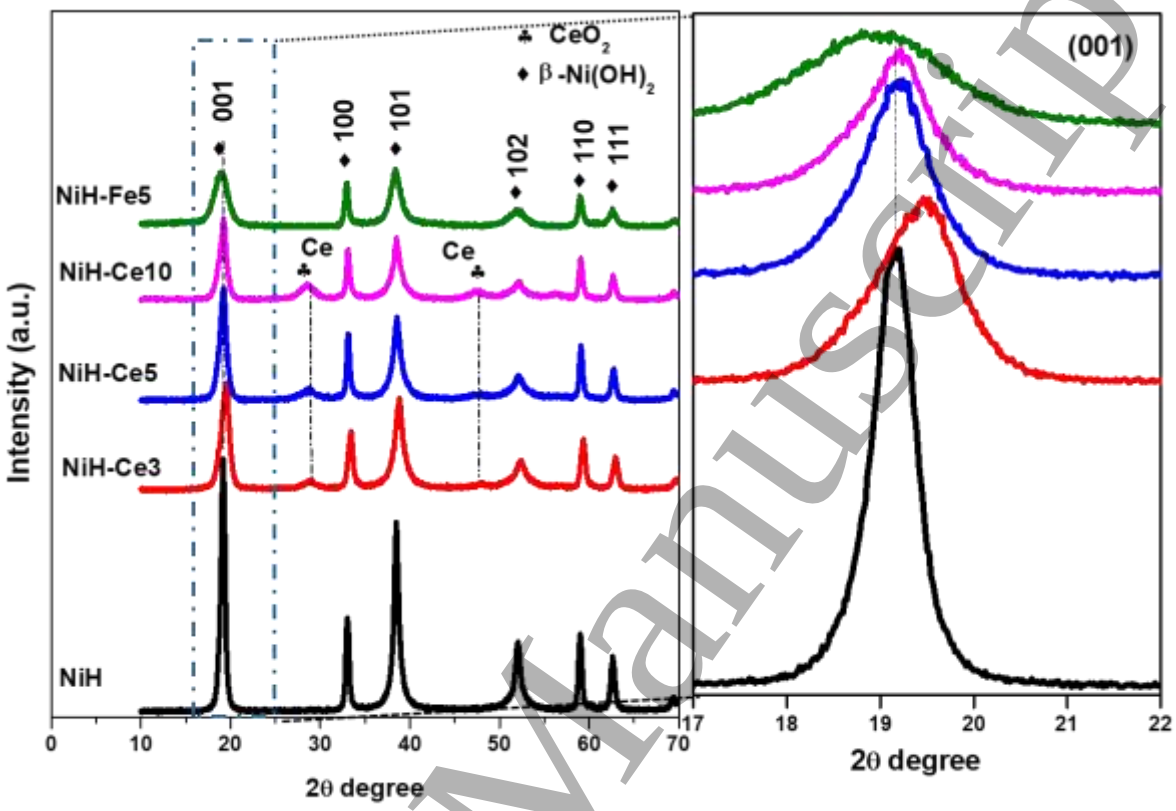

Fig. 2

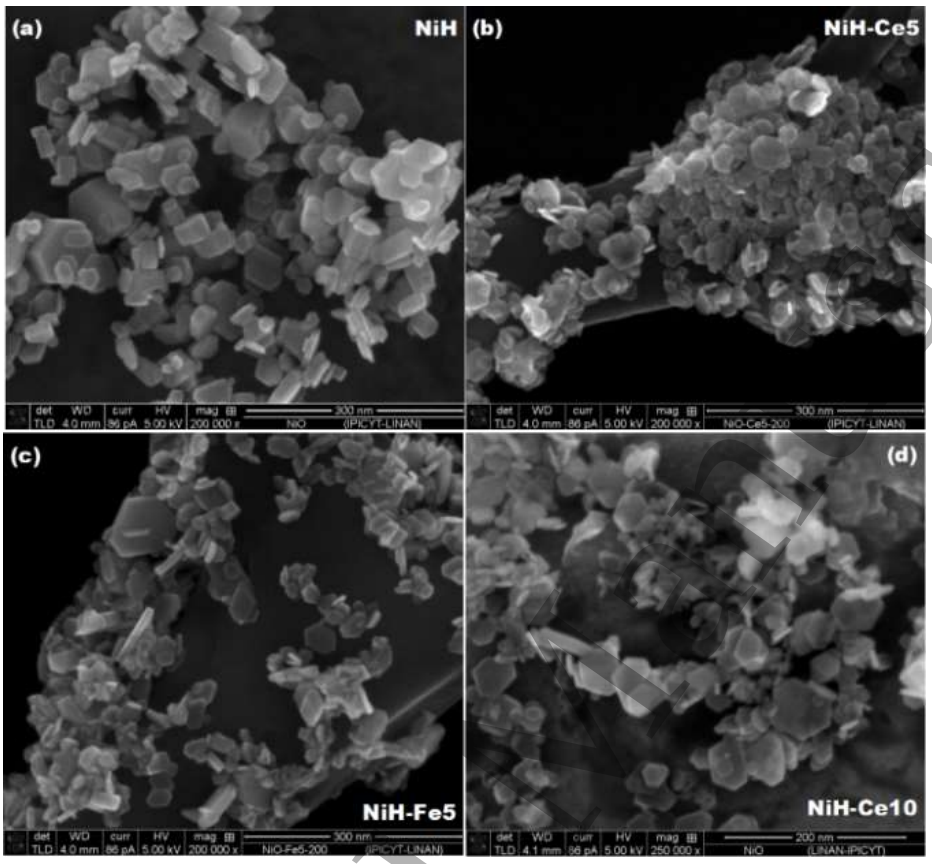

Fig. 3.

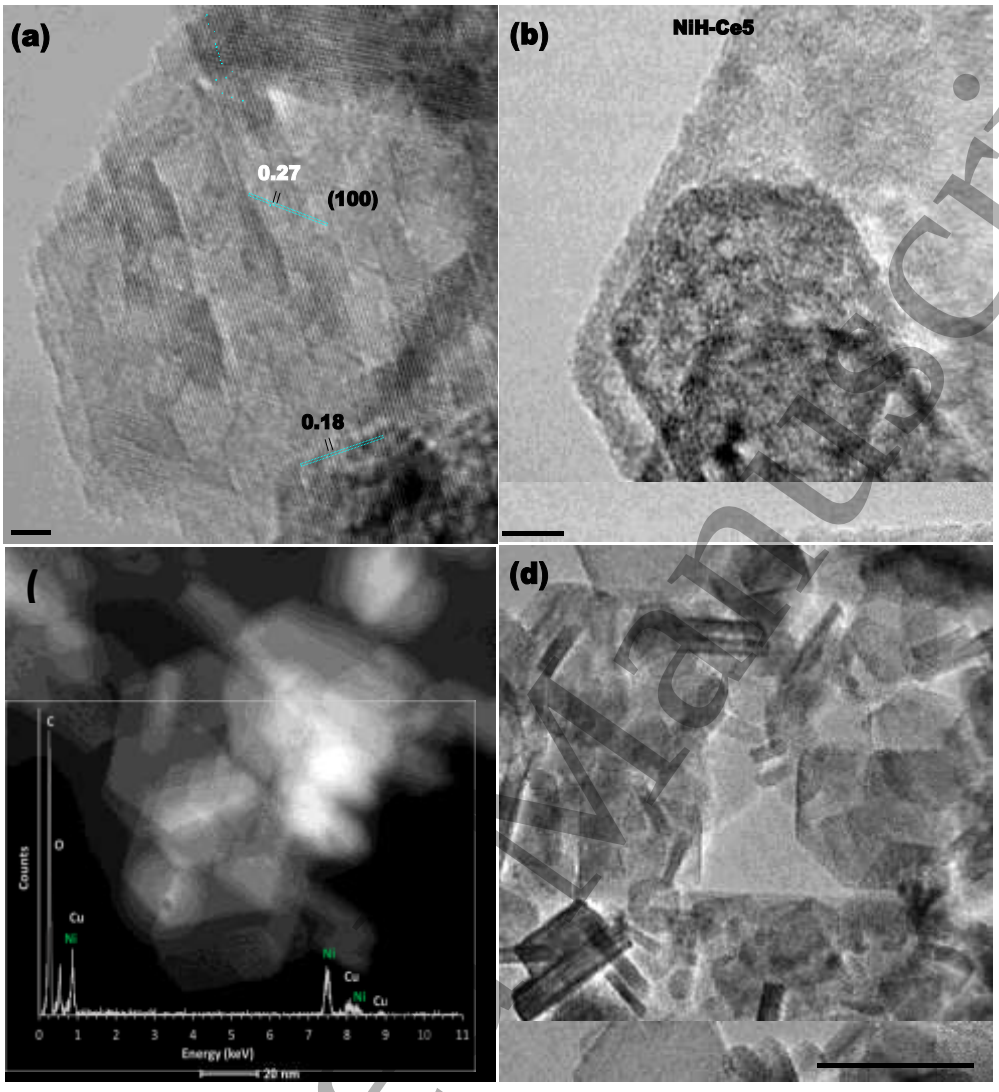

Fig. 4.

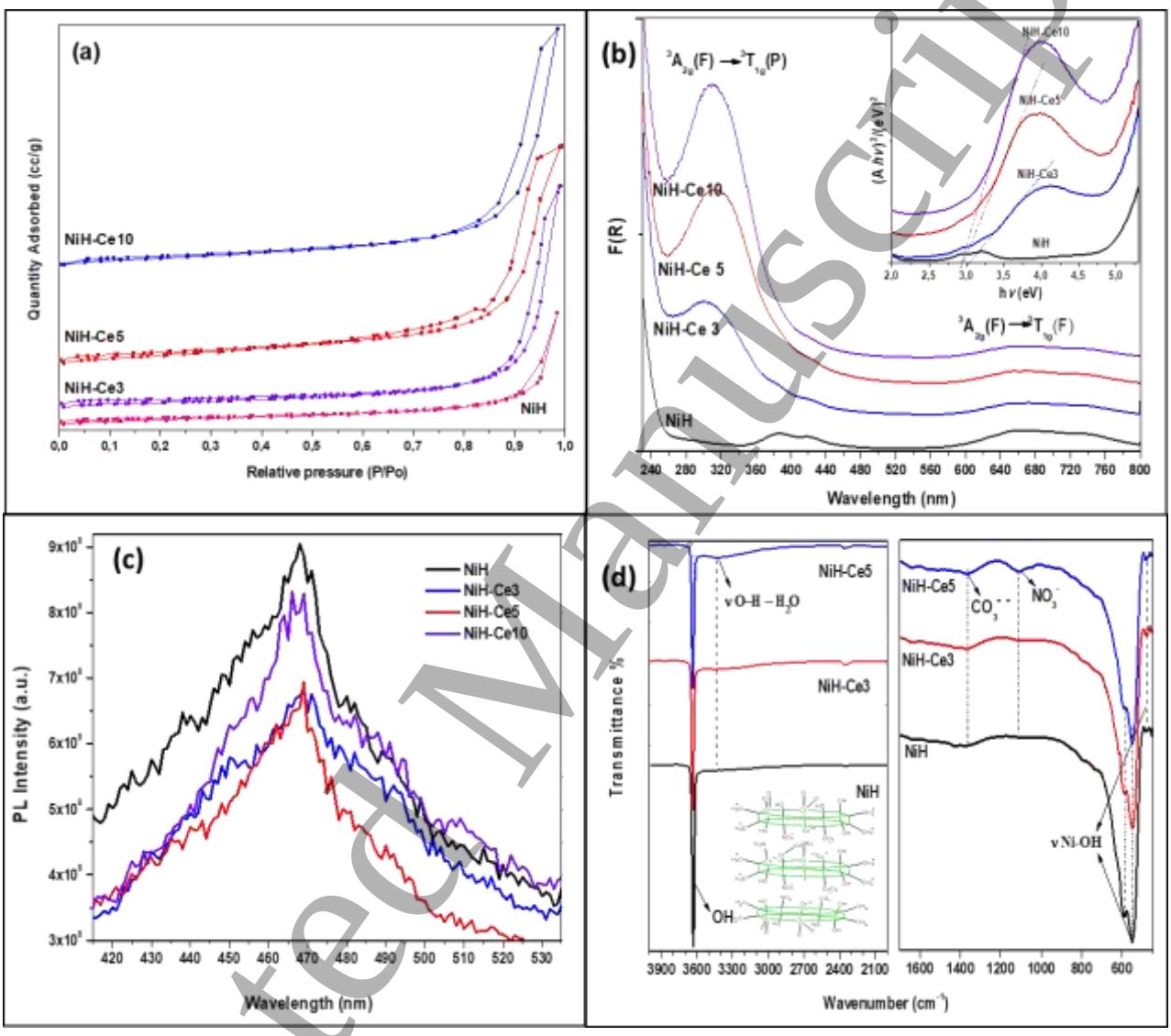

Fig. 5.

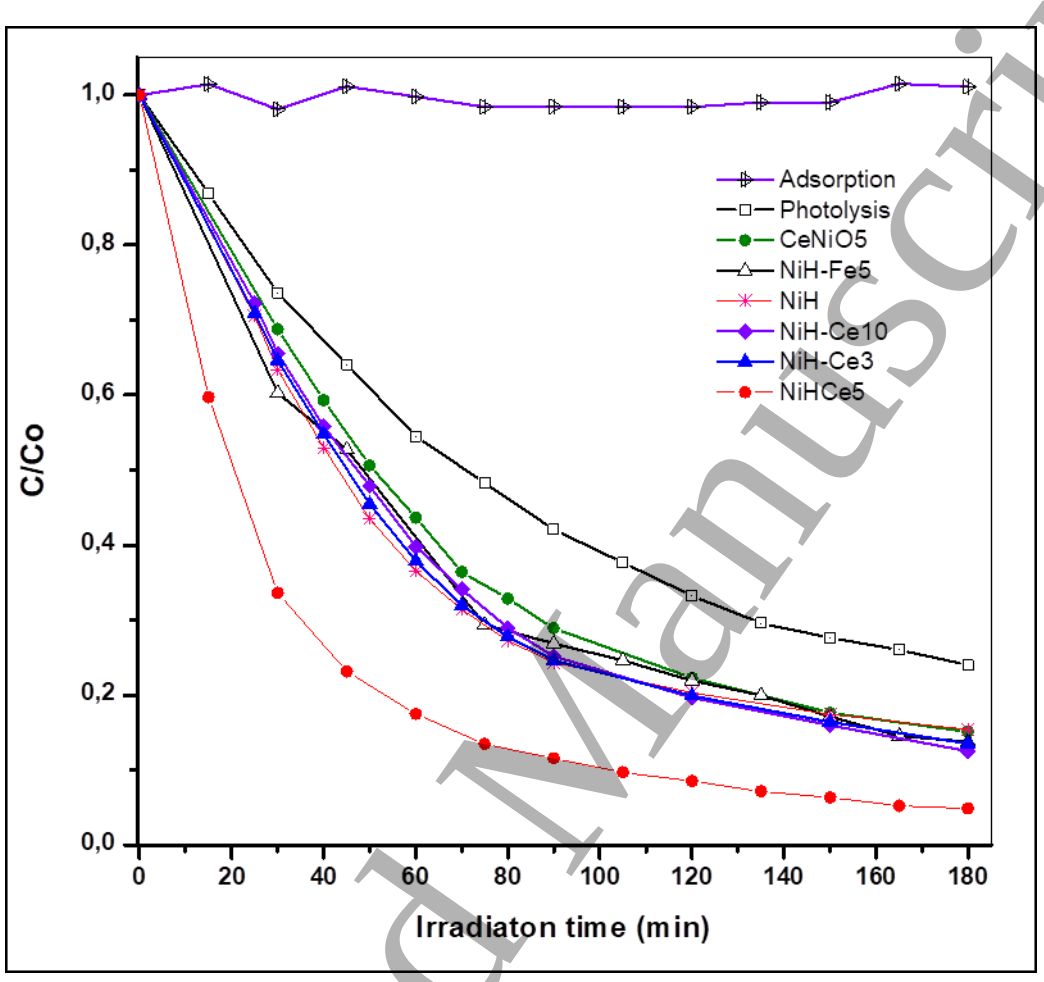

Fig. 6

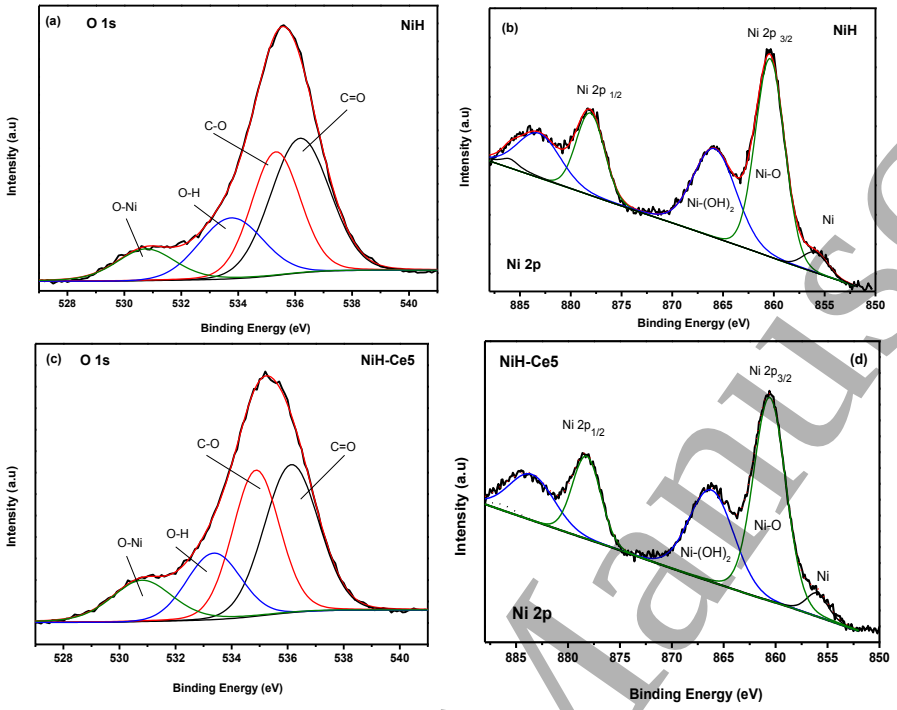

Fig. 7.

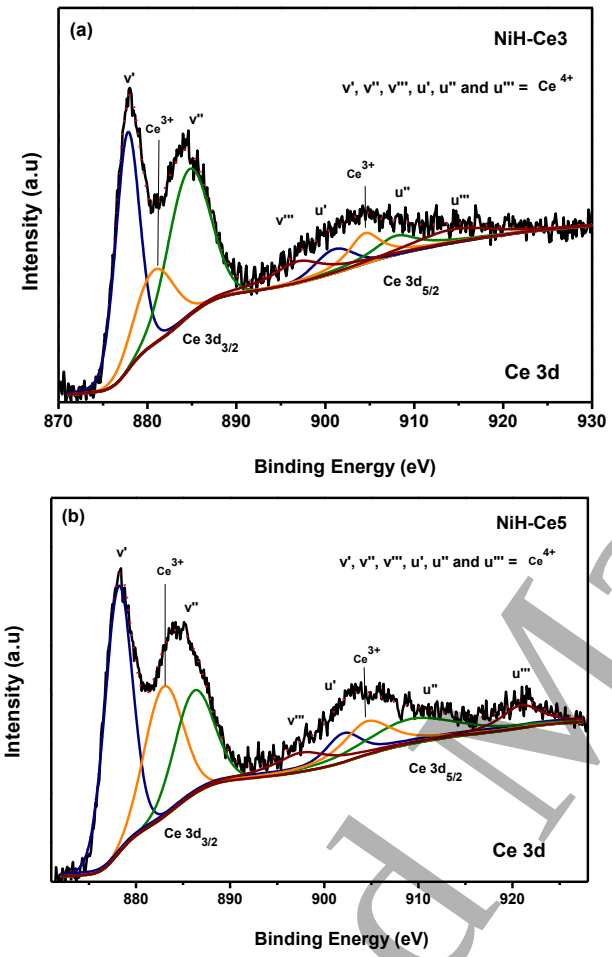

Fig. 8.

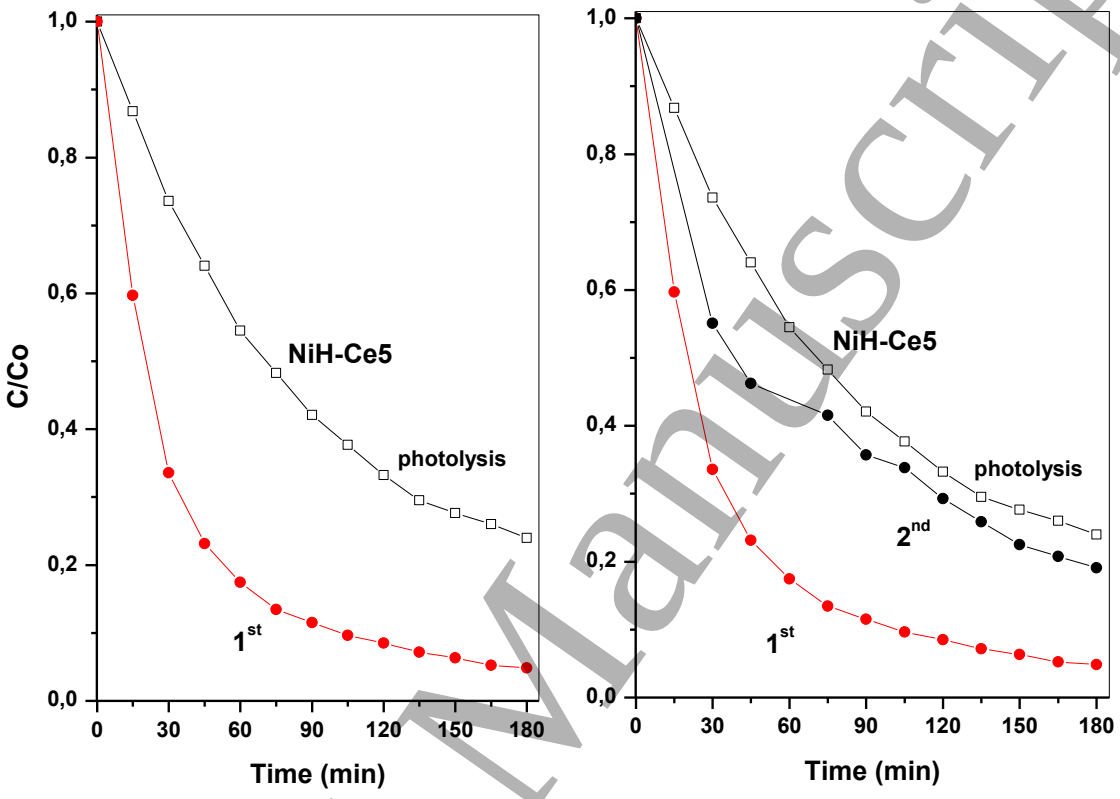

Fig. 9.

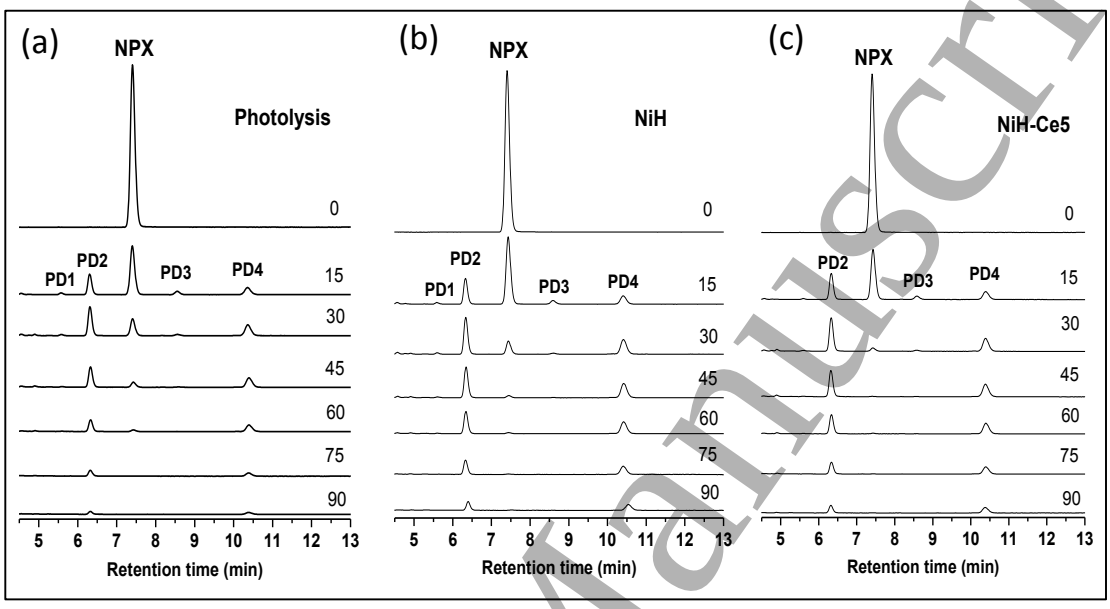

Tables

Table 1. Structural characteristics of nickel-layered hydroxides

photocatalyst	Crystallite size (nm)	d_{001}-spacing (nm)	Interlayer distance (nm)	Surface area (m^2g^{-1})
NiH	18.3	0.460	0.93	13.1
NiH-Ce3	10.9	0.457	0.91	26.6
NiH-Ce5	12.6	0.463	0.93	53.2
NiH-Ce10	12.0	0.462	0.96	47.8
NiH-Fe5	11.3	0.476	0.98	38.1

Table 2. Kinetic values of photodegradation and mineralization of different nickel hydroxides.

Photocatalyst	Reaction rate (x 10^{-2})	TOC (mgL^{-1})	Mineralization (%)
Photolysis	0.969	10.8	28
NiH	1.64	11.7	23
NiH-Ce3	1.62	11.3	25
NiH-Ce5	2.40	9.1	40
NiH-Ce10	1.57	10.9	27
NiH-Ce5 (cycle 1)	1.35	13.5	10

Table 3. Activity and selectivity values for the naproxen conversion over NiH and NiH-Ce5 catalysts and photolysis at different photoreaction times.

photocatalyst		Selectivity (%)				
	%C	NPX	PD1	PD2	PD3	PD4
NiH	99	**3**	**2**	**55**	-	**40**
NiH-Ce5	100	-	-	**57**	-	**43**
Photolysis	97	**15**	-	**49**	-	**36**